# The relationship between M and $M_L$ – a review and application to induced seismicity in the Groningen gas field, the Netherlands

Bernard Dost[1*], Benjamin Edwards[2] and Julian J. Bommer[3]

1. Royal Netherlands Meteorological Institute (KNMI), the Netherlands.

2. Department of Earth, Ocean and Ecological Sciences, University of Liverpool, U.K.

3. Department of Civil & Environmental Engineering, Imperial College London, U.K.

[*]Full address of corresponding author:

Royal Netherlands Meteorological Institute

Utrechtseweg 297

NL-3731 GA De Bilt

Netherlands

Email: bernard.dost@knmi.nl

# Abstract

The use of local magnitude ($M_L$) in seismic hazard analyses is a topic of recent debate. In regions of weak- or moderate-seismicity, small earthquakes (characterized by $M_L$) are commonly used to determine frequency-magnitude distributions (FMD) for probabilistic seismic hazard calculations. However, empirical and theoretical studies on the relation between moment magnitude (**M**) and $M_L$ for small earthquakes show a systematic difference between the two below a region-dependent magnitude threshold. This difference may introduce bias in the estimation of the frequency of larger events with given **M**, and consequently seismic hazard. For induced seismicity related to the Groningen gas field, this magnitude threshold is determined to be **M** ~ 2, with equality between **M** and $M_L$ at higher magnitudes. A quadratic relation between **M** and $M_L$ is derived for $0.5 < M_L < 2$, in correspondence to recent theoretical studies. While the seismic hazard analysis for Groningen is internally consistent when expressed in terms of $M_L$ (with the implicit assumption of equivalence between the two scales), a more physical interpretation of the seismicity model requires transformation of the earthquake catalogue from local to moment magnitude, especially since the dataset currently used in estimating time-dependent hazard consists mainly of $M_L < 2.5$ events. We show that measured station effects, derived from **M** calculations, correspond to predicted model calculations used to determine a ground-motion model for the region.



**Key words**: Induced seismicity, magnitude relations, hazard analysis

## Introduction

Seismic hazard assessment is usually concerned with earthquakes of magnitude 4 or greater, since smaller earthquakes generally produce ground motions that do not warrant consideration in engineering design (Bommer and Crowley, 2017). However, in the case of induced seismicity, smaller earthquakes can be important both because their effects are viewed as an imposed risk and also because they may occur in regions where buildings are designed and constructed without provision for lateral resistance against seismic shaking. In such situations, both seismicity models and ground-motion predictions are calibrated on small-magnitude earthquake data, the characterization of which—including the quantification in terms of magnitude—then becomes important. A particular challenge is to homogenize catalogues of induced earthquakes in terms of moment magnitude (Edwards and Douglas, 2014).

Gas production in the Groningen field in the northernmost part of the Netherlands is inducing earthquakes that potentially pose a threat to the built environment and to local inhabitants. As part of their response to the induced seismicity, a probabilistic seismic hazard and risk model (forming part of the production license application, or Winningsplan) is being developed for the Groningen field by the operator, Nederlandse Aardolie Maatschappij BV (NAM, 2016). In addition, and independently from the field operator, the Royal Dutch Meteorological Institute (KNMI) has developed a probabilistic seismic hazard model, which is compared to the Winningsplan model (Spetzler and Dost, 2017b; Dost et al., 2017). As part of the development of seismic hazard and risk models a site-specific ground motion model (GMM) has been developed for hazard assessment (Bommer et al., 2017a, 2017b). This model is based on finite-fault stochastic simulations, calibrated to accelerometer recordings from a local network in the region, and assumes that **M** = $M_L$ for $M_L$ > 2.5. The seismicity model, however, necessarily makes use of much smaller earthquakes and has invoked the implicit assumption of equivalence between local and moment magnitudes (Bourne *et al.,* 2014, 2015). Earthquakes used to develop the GMM have been located using a borehole network, established in the region in 1995 and recently extended (Dost et al., 2017; Spetzler and Dost, 2017a). Due to the expansion of the network in 2014, and the additional data this has provided for recent events, moment magnitudes can now be calculated to test the validity of the assumption that local and moment magnitudes are equal in the magnitude range of interest (**M** > 2.5).

Magnitudes of the induced earthquakes in the Groningen field are assigned by the official seismological service of the Netherlands, which is part of KNMI. These are local magnitudes, $M_L$. Within the context of the Groningen seismic hazard and risk models, both the compaction-based seismicity model (e.g., Bourne et al., 2014) and the ground-motion models (GMM) are being developed in terms of local magnitude but with the assumption of these magnitudes being equivalent to moment magnitude, **M**. Although this assumption represents a justified starting point (Deichmann, 2006), it has been a clear goal since the beginning of the project to either confirm this assumed equivalence or else to replace it with a validated relationship between the two scales.

In the first part of this paper we summarize how the two magnitude scales ($M_L$ and **M**) are defined and provide an overview of how the $M_L$ to **M** conversion issue has been addressed in other seismic hazard analysis projects. We then explore the specific case of Groningen, including an evaluation of local procedures at KNMI to determine magnitudes on both scales. We next provide a discussion of studies that have addressed the relationship between these two scales, including both empirical and theoretical publications. Finally, conclusions regarding the recommended procedures to be adopted for the Groningen hazard and risk assessments are summarized.

## *Magnitude Definitions*

Earthquake magnitudes provide a quantitative measure of size in terms of either a characteristic of the causative fault itself or the energy radiated from it. The two magnitudes that are the subject of this study, the local and moment magnitudes, are described in the following.

The local magnitude scale is defined by the peak displacement on the Wood-Anderson seismometer at a distance of 100 km from the earthquake. It is effectively a measure of the high-pass filtered displacement field. The local magnitude scale was originally defined by Richter (1935) using recordings of earthquakes in California. He proposed that:

$$M_L = \log_{10} A - \log_{10} A_0 \qquad (1)$$

with $A$ the peak amplitude on a x2800 gain Wood-Anderson torsion seismometer in mm, and $A_0$ a correction for attenuation with distance [such that $\log_{10} A_0(100\ km) = -3$]. The attenuation correction $A_0$ was determined by Richter (1935) for California, using a small dataset of recorded events and was limited to an epicentral distance range of 30-600 km. Boore (1989), using a much larger dataset, showed that systematic differences of up to 0.4 magnitude units can be obtained at short epicentral distances (0-30 km) if an appropriate attenuation function for the region is not derived. The Wood-Anderson seismometer was commonly used at the time to record regional and local seismicity. However, the instrument records ground motion displacement and acts as a high-pass filter above ~ 1 Hz. Therefore, the scale saturates for events larger than magnitude 7, where the displacement field is dominated by motions with frequencies below 1 Hz.

Despite the shortcoming of saturation at large magnitude, the local magnitude has been almost universally adopted as the magnitude of choice for regional earthquake observatories because it is easy and fast to calculate. Since the original scale was developed in California, where the geologic setting can be vastly different to other regions, most seismic observatories recalibrate the attenuation correction based on locally recorded seismicity. Whilst this should lead to a consistent magnitude scale, it typically does not, with regional differences becoming apparent where seismicity lies at the border regions of seismic networks (e.g., Fäh *et al.,* 2011). For instance, it is common for systematic differences between local magnitudes assigned by different agencies: the French network LDG typically estimates French-Swiss border region events to be 0.4 units higher than the Swiss Seismological Service. This is due to the simplistic nature of the attenuation correction, often lack of consideration of site effects and different interpretations of 'peak displacement'.

The moment magnitude is a measure of the size of the seismic moment ($M_0$) – representing work done – of an earthquake. The seismic moment has a physical definition that is based on the fault rupture surface area ($S$) and average displacement ($d$), and the shear modulus of the material (μ):

$$M_0 = \mu S d \quad (2)$$

Using the magnitude-energy relation:

$$\log_{10}(\mathrm{E}_s) = 1.5\mathrm{M}_s + 11.8 \quad (3)$$

and noting that $\mathrm{E_s}$ (in ergs) could be replaced by a measure of the strain work done, W (in dyn.cm), Kanamori (1977) proposed an extension to the surface-wave magnitude that did not saturate due to band-limited recordings:

$$\log_{10}(\mathrm{W}) = 1.5\mathrm{M_w} + 11.8 \quad (4)$$

Note here that $\mathrm{M_w}$ is not strictly a 'moment magnitude' (although often defined as such), rather a magnitude based on work done. Kanamori (1977) showed that under certain assumptions $\mathrm{W} = M_0/(2 \times 10^4)$, such that a magnitude, denoted **M**, could be directly related to the seismic moment. Extending this concept by also noticing the concurrence of the equation for $M_L$ in California (Thatcher and Hanks 1973), Hanks and Kanamori (1979) defined the moment magnitude, uniformly valid through $3 \lesssim M_L \lesssim 7$, $5 \lesssim M_s \lesssim 7½$, and $M_w \gtrsim 7½$ as:

$$\mathbf{M} = \frac{2}{3}\log_{10} M_0 - 10.7 \quad (5)$$

where $M_0$ is measured in dyn.cm ($10^{-7}$ N.m).

### ***Approach in Previous Projects***

Several seismic hazard projects over the last decade have faced the issue of magnitude scaling. The PEGASOS Project (Probabilistic Seismic Hazard Analysis for Swiss Nuclear Power Plant Sites; Abrahamson et al., 2002) was set up to assess the seismic hazard at nuclear power plant sites in Switzerland. As part of the project an update of the national earthquake catalogue was made (ECOS-02: Earthquake catalogue of Switzerland, 2002, Fäh et al., 2003), which in the case of no direct measure of **M** used a simple offset of -0.2 between $M_L$ and **M** based on analysis of a catalogue of moment tensor based **M** and corresponding $M_L$ in and around Switzerland (Braunmiller *et al.,* 2005). A subsequent project, which aimed to refine the results of the PEGASOS Project (the PEGASOS Refinement Project, or PRP; Renault et al., 2010), was undertaken between 2007 and 2013. As part of the project a revised earthquake catalogue was compiled (ECOS-09, Fäh et al., 2011). For this catalogue **M** was again assigned based on a scaling relation with $M_L$, but now using the curvilinear form of Goertz-Allmann et al. (2011).

The Central and Eastern United States Seismic Source Characterization for Nuclear Facilities (CEUS-SSC) project developed a homogenized earthquake catalogue for the US region east of the Rocky Mountains (USNRC*,* 2012). The catalogue contained relatively few $M_L$ and **M** pairs but they did observe that the data displayed the 'typical flattening of slope at the lower magnitudes' (USNRC*,* 2012). In order to avoid this issue, the data below $M_L$ 3.5 were not used in fitting the $M_L$ versus **M** model. Additionally, in order to convert $M_L$ to **M** the authors propose a number of different approaches depending on the data source and depending on the availability of data. These converted magnitudes were then in turn converted to **M** through more robustly determined conversion equations. This procedure, however, added significant uncertainty, with standard errors of 0.3 to 0.4 magnitude units.

The Thyspunt PSHA Project was a site-specific hazard analysis for a South African nuclear power station (Bommer et al., 2015). As part of the project a homogeneous earthquake catalogue was compiled, with magnitude in **M**. Since a wide range of magnitudes were available with both **M** and $M_L$, a South Africa specific conversion equation was developed.

The equation was developed giving strong preference to fitting the larger events with available moment tensors, whilst avoiding sharp jumps. This led to a correction that tends to overestimate **M** for smaller magnitudes (3 to 4) but since the minimum magnitude considered in the PSHA was 5.0, this was not considered important.

The Seismic Hazard Harmonization in Europe (SHARE) Project (Woessner et al., 2015) developed an earthquake catalogue for the European region. Due to the diversity of data sources (individual country seismic networks and observatories) different conversions were applied to $M_L$ to obtain **M**. The conversions are too numerous to describe in detail in this context, but can be found in Grünthal and Wahlstrom (2012) and Grünthal *et al.* (2013). However, the majority of conversions from $M_L$ relied on a linear scaling over a limited magnitude range.

## M and $M_L$ in Groningen

Since the north of the Netherlands was effectively aseismic before the onset of induced seismicity in the region in 1986, a local magnitude calibration had, up to that point, not been carried out. In fact, only one short-period station (WIT) had been in operation in the region since 1972 as part of the regional KNMI network.

### *Local Seismic Network*

Since 1988 a monitoring network was built-up in the north in two stages. First a small aperture array was installed around the city of Assen, consisting of short-period vertical sensors located at the surface and aimed at monitoring only one small gas field. Later seismicity spread over a larger area and a new borehole network was installed in 1995, equipped with 3-component sensors, replacing and extending the first array (Dost and Haak, 2007). In addition to the borehole monitoring network, a surface network was added consisting of accelerometers (Figure 1). Since 2014 the borehole network has been expanded over the Groningen gas field. Boreholes consist of 4 levels of sensors at a maximum depth of 200m and each borehole is also equipped with a surface accelerometer (Dost et al., 2017).

### *Local Magnitudes in Groningen*

In the period 1986-1992 only 6 events occurred in the north of the Netherlands, with one of them in the Groningen area. Local magnitudes were calculated using a reference station of the KNMI network (WTS), at an epicentral distance of 100-150km. The attenuation relation developed by Ahorner (1983) was used in the calculations (Eqn. 1), where $\log A_o = -1.90 \log(R) - 0.35$, with $R$ being the hypocentral distance. The Assen array allowed the calculation of a first attenuation relation for the north of the Netherlands, although unfortunately only vertical components were available. In 1991 an experimental borehole station FSW was installed, east of the Groningen gas field, with four levels of 3 component geophones at 75m vertical spacing. Data from the geophones at 225m depth were subsequently used to determine magnitudes by extrapolation of the previously determined attenuation function.

After the borehole network became operational in 1995, a more detailed calibration became possible for a larger region, including the Groningen gas field. The calibration was undertaken by KNMI, and is summarized here. Following Kanamori et al. (1993) the attenuation function for the North of the Netherlands was modeled using:

$$q(R) = c\,R^{-n} e^{-\alpha R} \tag{6}$$

which includes effects of geometrical spreading, attenuation, reflection and refraction and scattering and is regarded as a reasonable description for the average trend over short epicentral distances (in our application: 0-80 km). Since there were existing estimates of $M_L$, a search for values of parameters c, n and $\alpha$ was performed by minimizing the function:

$$\phi = \sum_{j=1}^{N} \sum_{i=1}^{M} |\log A_{i,j} - M_{L_i} - \log q(R_j)|^2 \tag{7}$$

$$M_{L_i} = \frac{1}{N} \sum_{j=1}^{N} M_{L_{i,j}}$$

where index *i* refers to the event and *j* to the recording station and *A* is the average maximum Wood-Anderson (WA) simulated amplitude (half peak-to-peak) of the horizontal components. There is a trade-off between *n* and $\alpha$, which was noted by several authors (e.g. Bakun and Joyner, 1984; Savage and Anderson, 1995). An iterative grid search was carried out: after an initial estimate of the attenuation function, new values for $M_L$ were calculated and a new minimization performed to refine the estimate of the attenuation function. By fixing the value for n and solving for α, a steady decrease of α with increasing n was observed, coinciding with a decrease in the minimum of the misfit function. It is important to emphasize that amplitudes are always measured at the deepest level in the boreholes (generally 200 m, except for FSW where it is 225 m). Based on a dataset of 157 records, recorded in 1995 and the first half of 1996, the minimization of Equation (7) led to:

$$\log_{10} A_0 = -1.33 \log(R) - 0.00139\, R - 0.424 \tag{8}$$

(Dost et al., 2004). The first term implies that geometrical spreading is faster than the usual assumed $1/R$ and from the second term an average $Q$ = 280*$f_{WA}$ (for β=3.5 km/s) can be derived (Bakun and Joyner, 1984), with $f_{WA}$ being the dominant frequency of the measured WA displacements. The attenuation function applies to a larger region than only the Groningen area, since the network also covers many small gas-fields. The difference between the magnitudes calculated using the attenuation function based on the Assen array data and re-calibrated magnitude estimates is small, around 0.1-0.2 magnitude units. In addition station corrections have been calculated and are less than 0.1 magnitude units. Due to the limited dataset, sampling only part of the region, and small values of the station corrections compared to the uncertainty in $M_L$ (between 0.2-0.3), it was decided not to use them in the magnitude calculations.

Equation (8) was used in determination of local magnitudes used here. Figure 2 shows the variation in magnitude calculated for each individual station with respect to the average magnitude for events recorded in the period 2010-2015. For hypocentral distances ($R$) less than 10-15 km, a distance dependence is observed and a correction of the attenuation relation at short distance may be considered as also found in other regions (e.g., Edwards *et al.,* 2015; Butcher et al., 2017). However, this distance dependence is small with a mean residual of 0.12 magnitude units for $R$ < 10 km, while the standard deviation at the shorter distance bins is high (0.15-0.23 magnitude units).

## *Moment magnitude*

Seismic moment, $M_o$, can be derived from the spectra of P and S waves. In this study the focus is on S waves, which typically have a higher amplitude and are therefore still relatively noise-free for weak events. The S-wave displacement spectrum $A(f)$ recorded in one station can be written as the product of a source term, $\Omega(f)$, an attenuation term, $D(R, f)$ and a site effect term, $S(f)$:

$$A(f) = \Omega(f)D(R, f)S(f) \tag{9}$$

where $R$ is the hypocentral distance, $f$ is frequency. As a source model, the (Brune 1970, Brune 1971) model is chosen, as modified by Boatwright (1978):

$$\Omega(f) = \frac{\Omega_0}{\left(1+\left(\frac{f}{fc}\right)^{\gamma n}\right)^{1/\gamma}} \tag{10}$$

Abercrombie (1995), de Lorenzo *et al.* (2010) and others found that $\gamma$=2 and n=2 produces a better model for spectra of local earthquakes compared to the standard Brune model with $\gamma$=1 and *n*=2. A test of model fit to the data showed that this also applies to the current dataset. It should be noted, however, that the result depends on the selected events, so either model is arguably suitable. For instance, in the development of the GMM for Groningen (Bommer et al., 2017b), the Brune model was assessed to provide a marginally better better fit to larger (M > 3) events.

The low-frequency spectral level $\Omega_0$ can be expressed in terms of seismic moment $M_0$:

$$\Omega_0 = \frac{2\Phi}{4\pi\rho_0^{\frac{1}{2}}\rho_S^{\frac{1}{2}}v_0^{\frac{1}{2}}v_S^{\frac{5}{2}}}g(R)M_0 \tag{11}$$

where $\Phi$ denotes the average radiation, which is taken as 0.64 for shear waves recorded at close distances at a 60 degrees dip-slip fault (Boore and Boatwright, 1984), $\rho_s$ the density at the source (2.6 kg/m$^3$) and $\rho_0$ density at the surface (2.1 kg/m$^3$), updated from Kraaijpoel and Dost (2013), $v_s$ the shear velocity at the source (2009 m/s, pers. comm. Remco Romijn) and $v_0$ shear velocity at the surface (which over the field has an average value over the uppermost 30 m of 200 m/s; Kruiver et al., 2017). The free-surface effect is introduced as a factor of 2, which is exact for near vertical incoming SH waves and, in general, a reasonable estimate for vertical incoming SV waves. The function $g(R)$ describes the geometrical spreading and is discussed in detail later. Attenuation along the path from source to receiver involves anelastic decay (e.g., Drouet *et al.,* 2010) and high-frequency damping:

$$D(r,f) = e^{-\frac{\pi R f}{Q v_{sa}}} e^{-\pi \kappa f} = e^{-\pi f t^*} \tag{12}$$

with $t^* = \frac{R}{Q v_{sa}} + \kappa_0$

where $v_{sa}$ is the average shear velocity between source and receiver; $Q$ is the damping parameter and in these calculations assumed to be frequency independent; $S(f)$ is the site effect. Combining equations (9) and (11) to (12), the S-wave spectral displacement can be written as:

$$A(f) = \Omega_0 \frac{S(f)}{\left(1+\left(\frac{f}{fc}\right)^4\right)^{1/2}} e^{-\pi f t^*} \tag{13}$$

A grid search was carried out to determine the best fitting parameters for $f_c$, $t^*$ and $\Omega_0$ and to calculate $M_0$. This grid search was carried out using a minimization function:

$$\sigma^2 = \frac{1}{N}\sum_{j=1}^{N}\left|\log\left(A^{obs}(f_j)\right) - \log\left(A^{calc}(f_j)\right)\right|^2 \tag{14}$$

For each event, the spectrum of each station is processed separately, since this will give insight regarding the variability of the estimated parameters. Moment magnitude is calculated using Equation (5) where:

$$M_0 = \frac{4\pi \rho_0^{1/2} \rho_s^{1/2} v_s^{5/2} v_0^{1/2}}{2\Phi g(R)} \Omega_0 \tag{15}$$

This formulation assumes that the site effect term $S(f) = 1$, with frequency-independent amplification included in Equation (15) by accounting for the impedance contrast between the source and site.

## ***Data and processing***

The Groningen accelerometer network has developed over the years from a sparse stand-alone triggered system to a dense continuous recording system. The former consisted of SIG SMACH instrumentation (Dost and Haak, 2002), while the latter is equipped with Kinemetrics Episensor accelerometers and Basalt dataloggers. The triggered systems provide output in cm/s$^2$, while the Episensor data needs a conversion from digital counts. This conversion factor is 4.7684e-7 g/C and the response is flat for acceleration within the frequency range of interest.

The data processed in this paper have been recorded in accelerometer stations of the Groningen network. The number of stations that could be used varies in time and also depends on event location. Data are sampled at 5 ms time intervals and recorded in real time as continuous mini-seed volumes and transferred over the Internet using the seedlink protocol. A time window of 512 samples (2.56s) around the S-onset was selected for processing. A Hanning window was applied prior to the Fourier transformation. Based on the signal-to-noise ratio of most records, the frequency range used to fit the measured spectra to the model is limited to a maximum range of 1-30 Hz (e.g. Figure 3).

The geometric mean of the spectra of the horizontal components is used in this analysis, compatible with the development of the GMM for Groningen (Bommer *et al.,* 2017a, 2017b). In the process of spectral fitting a strong correlation between corner frequency, $f_c$, and attenuation, $t^*$, is observed. The estimate of the low-frequency part of the spectrum, $\Omega_0$, is much more stable and is the only parameter required for calculation of **M**.

### *Geometrical spreading*

In Equation (11) the geometrical spreading is often assumed to be well described by a simple $g(R) = 1/R$ relation. However, in the attenuation relation derived for the $M_L$ calculation, a higher attenuation was found $g(R) = 1/R^{-1.33}$. For magnitude calculations this parameter is of crucial importance. For example, Drouet et al. (2005) modeled geometrical spreading by:

$$g(R) = \frac{1}{R_0}[\frac{R_0}{R}]^{\lambda} \tag{16}$$

where $R_0$ is equal to a reference distance. Since for the low frequency part of the spectrum:

$$\log\left(A(r,f\rightarrow 0)\right) = \log\left(\frac{2\Phi M_0}{4\pi\rho_0^{1/2}\rho_s^{1/2}v_s^{5/2}v_0^{1/2}}\right) + \log\left(S(f\rightarrow 0)\right) - \lambda\log\left(\frac{R}{R_0}\right), \qquad (17)$$

parameter λ can be estimated from the distance dependence of measured $\Omega_o$ values. In this procedure $R_0$ = 1000 m. For the determination of an average geometrical spreading factor for Groningen, events of different magnitudes are compared by scaling the logarithm of the low-frequency part of the spectrum with the logarithm of the averaged seismic moment for each event. Results are shown in Figure 4. Linear regression gives the best fitting line:

$$\frac{\log\left(A(r,f\rightarrow 0)\right)}{\log M_0} = (-1.89 \pm 0.08)*\log\left(\frac{R}{R_0}\right) - (16.88 \pm 0.07) \qquad (18)$$

Figure 4 shows the results of the regression including the 95% confidence limits. An average geometrical spreading factor λ= 1.9 has been adopted from these data. A major source of error in these measurements is the effect of the radiation pattern and possible site effects. Therefore, comparison with model calculations is important. Results from finite difference, isotropic wave equation modelling are shown in Figure 5. A clear difference in geometrical spreading is observed for the hypocentral distance range 3-7 km and 10-14 km. It should be noted that this modelling is performed for elastic media. The average geometrical spreading derived from the normalized low-frequency spectra is in line with the modelling results.

For all events a general λ= 1.9 is used for each station in the calculation of **M**. However, for the Garmerwolde event (2014-09-30), with location in the south-west part of the field, this choice for geometrical spreading results in a clear increase of magnitude with distance.

Consequently, for this event only, recordings at epicentral distances < 10 km have been used in the analysis.

### *Comparison of M*

In order to explore the sensitivity of event-to-event variability in calculated **M** depending on the approach we also calculated **M** using the approach detailed in Edwards et al. (2010). Identical material properties were assumed in both methods. The primary difference is the spectral fitting method and the use of distance-dependent (segmented) geometrical spreading (for more detail: Edwards et al., 2010) and site effects are determined as part of the joint inversion. In this method, the entire S-wave train is taken as signal and an 'apparent' geometrical decay determined. This rate of decay was found to be $1/R^{1.58}$ from 3 to 7 km, and $1/R^{0.09}$ from 7 to 12 km, which has similar form to the synthetic results (Figure 5), but has an overall lower slope due to the inclusion of multiple S-phases. Nevertheless, the resulting **M** values are very similar and follow a 1:1 trend with the previously calculated values (Figure 6).

### *Relationship between M and $M_L$*

A total of 116 events, listed in Table S1, available in the electronic supplement to this article, have been processed to calculate **M** and to compare these values to measured $M_L$. In general the uncertainties in $M_L$ are larger than uncertainties in **M.** This may be caused by the fact that the original borehole network has a large inter-station distance, on average 20 km, while covering a heterogeneous upper crustal structure. The distance between the accelerometer stations is less and, being located at the surface, do include the highly heterogeneous uppermost 200m.

For events of magnitude $M_L$>2 both magnitudes are similar (Figure 7). For smaller events a quadratic relation was fit to the data using a least-squares optimization:

$$\mathbf{M} = 0.056262 * M_L^2 + 0.65553 * M_L + 0.4968 \quad \text{for } 0.5 \leq M_L \leq 3.6 \qquad (19)$$

This relation is close to the relation derived by Grünthal et al. (2009). Edwards (2015), Munafò et al. (2016) and Deichmann (2017) showed that for small events $\mathbf{M} = 2/3 * M_L + C$. In Figure 7 this relation is close to the quadratic fit for small events ($M_L < 1.5$) with C=0.53.

These results confirm the validity of the assumed equality between **M** and $M_L$ for $\mathbf{M} \geq 2.5$. However, since the seismicity in the region is non-stationary, time dependent b-values are required in the hazard analysis, based mainly on $M_L < 2.5$. Therefore measured $M_L$ values should ideally be converted to **M** before a reliable *b*-value can be determined (Deichmann, 2017; Spetzler and Dost, 2017b).

### *Site effects*

The calculated moment magnitudes are averages over multiple stations. Site effects can be derived from an analysis of the magnitude residuals at each individual station (Edwards et al., 2013). All stations in operation have been processed and the majority showed a mean residual around zero, except for two stations: BHKS and BAPP (Figure 8).

For the Groningen region a site-specific ground motion model has been developed (Bommer et al., 2017b). For this model, amplification functions have been derived based on 1D site response analyses (Rodriguez-Marek et al., 2017). Figure  shows the frequency-dependent amplification functions calculated at the location of the stations shown in Figure . A pronounced amplification effect at ~ 2Hz for stations BHKS and BAPP, visible in the blue (empirical) or red (theoretical) lines in Figure 10, corresponds to the observed higher magnitude residual. This amplification effect has not been observed at the other stations. Since the magnitude dataset is still small, the analysis could not yet be carried out for the new borehole network.

## Discussion: the relation between M and $M_L$

### *Empirical Data*

Since both local and moment magnitudes are often directly determined for moderate sized earthquakes (4 < **M** < 6), there is the opportunity to observe, empirically, the relationship between the two—as shown for events in Groningen. Unfortunately, the magnitude range over which both magnitudes are available is often rather small due to the fact that moment tensor analyses (used to calculate **M**) require long-period waveforms (e.g., T > 10 s). For earthquakes below **M** = 4, these periods are typically dominated by noise. Some studies, as here, extend the lower limit of moment magnitude determination using spectral analysis techniques. A limitation in this case is that since short-period motions are analysed, there is a higher degree of uncertainty and the risk of biased estimates, for example due to local site amplification effects. Furthermore, methodological differences between approaches can lead to systematic bias in estimated magnitudes. Nevertheless, by using two independent methods for the calculation of **M** we show that the analysis for the Groningen data is robust.

There are numerous studies comparing regional $M_L$ and **M**. Often a shortcoming of such studies is the limited magnitude range available: regions of low seismicity, such as Northern Europe tend to focus on smaller magnitude data, using spectral analyses to obtain **M** from short-period data, while regions of higher seismicity tend not to compute (or provide) moment magnitudes for smaller events. Authors therefore often use a simple linear regression (straight line fit) between the two magnitudes. Figure 10 shows a collection of such regressions. Only models presented by Grünthal et al. (2009) and Edwards et al. (2015) span a wide magnitude range. Grünthal et al. (2009) use data from accross Europe, while Edwards et al. (2015) use data from Switzerland and central Europe in addition to theoretical considerations on scaling.

Authors have, in the past, assumed that **M** = $M_L$ or that **M** = $M_L$ + C. As seen in Figure 10, this is a reasonable average assumption for **M** > 2.5. Most models predict smaller **M** than $M_L$ in this range (with offsets of ~ C = -0.1 to -0.4). Below $M_L$ ~ 2.5, **M** tends to be systematically higher than $M_L$. However, individual regions show significant systematic differences, even for M > 2.5.

Due to the limits of computing **M** across a wide range of magnitudes, there are few studies that span the 'complete' range of magnitudes and investigate the magnitude dependence of the $M_L$ versus **M** scaling. An early example was that of Hanks and Boore (1984). They saw the variety of different scaling relations, even in the California region, as evidence that the results depended on the chosen magnitude range. By analysing earthquakes between $M_L$ = 0 and 7 in California from a number of sources they observed a curvilinear relationship between $M_0$ (and consequently **M**) and $M_L$. Grünthal et al. (2009) produced an earthquake catalogue for central, northern, and north-western Europe. Based on this they observed a quadratic trend between **M** and $M_L$. Similarly Edwards et al. (2010) used Swiss and central European (Italian, French, Austrian and German) events to develop empirical relationships between $M_L$ (assigned by the Swiss Seismological Service) and **M** calculated based on spectral analysis. Following Edwards et al. (2010), Goertz-Allmann et al. (2011) expanded the Swiss dataset to include events of smaller magnitude, and used moment tensor solutions for **M** where available. They defined a piecewise relationship (linear to $M_L$ = 2, quadratic between $M_L$ = 2 and 4 and 1:1 scaling with **M** above $M_L$ = 4) to avoid the problem of sparse data at low and high magnitudes. Edwards et al. (2015) revised this model to account for new data ($M_L$ < 2) and the theoretical scaling of M $\propto$ 2/3 $M_L$ for small (M < 2) events (Deichmann, 2017).

### ***Simulation- and Theoretical-based Studies***

Deichmann (2006) proved that **M** $\propto$ $M_L$ in the absence of attenuation and neglecting the effect of the Wood-Anderson response, which only affects large magnitude (low-frequency) events. He did this by showing that as the seismic moment increases two things happen to the radiated displacement pulse: its duration increases, and its peak amplitude increases. The duration of the pulse is directly linked to the size of the rupture, which can itself be related to the seismic moment and the static stress drop. After accounting for the increase in displacement pulse duration due to fault growth, it is shown that the peak-amplitude must increase as $2/3\log M_0$. Since **M** also increases with $2/3\log M_0$, it can be inferred that **M** = $M_L$ + C. In practice therefore, assuming suitably calibrated scales, **M** = $M_L$. This initial theoretical analysis did not explain empirical observations of a break in 1:1 scaling at low magnitude. Deichmann (2006) argued that this could be due to two issues: the effect of anelastic attenuation Q, or the instrument response. Time-domain simulations for a realistic Q model with or without convolution with a Wood-Anderson instrument showed that for increasingly small **M**, the difference between $M_L$ and **M** increases, just as in the empirical analyses. For small events the influence of Q is dominant. Deichmann (2017) and Munafò et al. (2016) expanded on this to show that there is a sound theoretical basis for the scaling of small events (approximately $M_L < 2$) of the form: $M_L = 3/2*\mathbf{M} + C$.

In addition to time-domain simulations, random vibration theory (RVT) can be used to simulate the response of a Wood-Anderson seismometer to input ground motion. This was the method used by Hanks and Boore (1984) to explain the curvature of the $M_L$:**M** data observed in their empirical analysis. Edwards et al. (2010) showed a number of examples using this approach, with different input ground motion (defined by **M**, stress-drop and Q). They showed that the form of the curvature was explained by different Q values (or equivalently site $\kappa_0$) at the low magnitude range, with the shape in the high-magnitude range (**M** > 5) defined by the stress-drop (and Wood-Anderson instrument response).

The theoretical and simulation based analyses of Deichmann (2006, 2017), Edwards et al. (2010) and Munafò et al. (2016) support the conclusion of Hanks and Boore (1984) that the scaling of $M_L$ and **M** is due to a complex interaction of the earthquake source, wave-propagation and the response of the Wood-Anderson seismometer. The fact that Groningen events are not out of the ordinary compared to various regions with more typical seismicity, given the very particular seismo-tectonic conditions in and around the Groningen gas field, could be considered somewhat surprising. At the low magnitude range, the higher attenuation in Groningen (due to thick low velocity deposits, such as peats), implies that the equivalence between **M** and $M_L$ should break down at higher magnitudes than normal (Deichmann, 2017). However, if Groningen events are of lower stress-parameter than other regions (i.e., Groningen events average 5 – 7 MPa compared to typical values of 10 MPa Bommer et al., 2017b), this would counteract the attenuation effect: events of a particular magnitude are already of lower-frequency content and attenuation therefore has a reduced impact.

## Conclusions

Numerous empirical studies have shown that 1:1 scaling between $M_L$ and **M** does not extend to low magnitudes. For $M_L > 2$ - 3, the average of the studies seems to conform with **M** $\approx M_L$, albeit with significant scatter of the scaling relations between individual regions. For $M_L < 2$, in studies spanning a broader magnitude range, it is observed that **M** $> M_L$. The difference, furthermore, tends to increase for increasingly small magnitudes, with up to a unit of difference for $M_L = 0$ events. Three studies compiling data over a broad magnitude range: in Europe, Switzerland and neighboring regions, and in California, show a distinct curve in the $M_L$ versus **M** scaling below $M_L = 2.5$.

This is consistent with simulation-based studies (Deichmann, 2006, 2017; Edwards et al., 2010; Hanks and Boore, 1984; Munafò et al., 2016), which show that when accounting for the effect of attenuation (Q and $\kappa_0$) *and* the Wood-Anderson instrument response, we should expect a curvilinear scaling relation between $M_L$ and **M** over a wide magnitude range. This is due to a complex interaction of the earthquake source signal and the filtering effects of the propagation medium (low-pass) and instrument response (displacement high-pass).

Due to the strong regional dependence of $M_L$ assigned for a given earthquake (e.g., Fäh et al*.,* 2011) coupled with the limited datasets containing both $M_L$ and **M**, regional correlations calibrated over limited magnitude ranges are usually applied in PSHA projects. Since it is known that the scaling should not be linear, this means that such conversions are only valid between the range of magnitudes in which they were derived. Given a suitable seismological background model (e.g., Atkinson and Boore, 2006; Edwards and Fäh, 2013; Rietbrock et al*.,* 2013), the expected scaling can be simulated. This has been performed for the Groningen GMM (Bommer et al., 2017b) (Figure 11). This model provides further confirmation that for stress drops ~10 MPa, $M \approx M_L$ for $M_L > 2.5$ but indicates a somewhat stronger saturation at lower magnitudes ($M_L < 1.5$) (perhaps due to the fact that we have limited events for the empirical analysis). However, such models are known to be non-unique and, consistent with good practice in PSHA, the epistemic uncertainty of the correction should also be carefully considered.

The **M**-$M_L$ relation for Groningen is close to the relation Grünthal et al. (2009) published for the central, northern and northwestern Europe. However, Edwards and Douglas (2014) showed a large variation in published catalogue magnitudes with respect to **M** for induced earthquakes worldwide, demonstrating the need for a proper definition and calibration of magnitudes for each region of interest rather than simply assuming concurrence with a continental-scale model. In the Groningen case it has been shown that **M** is approximately equal to $M_L$ above $M_L = 2.5$, confirming the assumption of equality between the magnitude scales in the hazard assessment for induced seismicity in the region. A systematic trend, best described by a quadratic relation between **M** and $M_L$ and similar in form to those observed in other empirical and theoretical studies, is seen for magnitudes below $M_L = 2.5$. This trend is used to correct $M_L$ when estimating time-dependent *a*- and *b*-parameters derived from the frequency-magnitude relation for Groningen, which are mainly based on $M_L < 2.5$ (Spetzler and Dost, 2017b). In contrast to the findings of Edwards et al. (2015) and Butcher et al. (2017), the effect of geometrical spreading at short distances for Groningen, derived from the distance dependence of the low-frequency part of the spectra, deviates significantly from 1/R. Results of a comparison of **M** station residuals with independent empirical and theoretical model predictions show a good correlation, and can be considered an independent check of the quality of the model predictions.

## Acknowledgements

We are grateful to Gert-Jan van den Hazel and Jordi Domingo-Ballesta for giving efficient access to the data. The second and third authors wish to express thanks to Jan van Elk from NAM for support to undertake this work. The work presented in this paper has benefited from informative discussions with several individuals including Steve Oates, Jesper Spetzler, Ewoud van Dedem and Thomas Piesold. We are also very grateful to Associate Editor John Ebel, to Hilmar Bungum and to an anonymous reviewer for constructive and encouraging feedback on an earlier version of this manuscript.

## Data and Resources

The data used in this work are available at the KNMI Seismic and Acoustic Data Portal (http://rdsa.knmi.nl/dataportal/).

## References


Abercrombie, R.E. (1995) Earthquake source scaling relationships from -1 to 5 $M_L$ using seismograms recorded at 2.5 km depth, *J. Geophys. Res.* **100**, 24015-24036.

Abrahamson, N.A., Birkhauser, P., Koller, M., Mayer-Rosa, D., Smit, P., Sprecher, C., Tinic, S. & Graf, R. (2002). PEGASOS – A comprehensive probabilistic seismic hazard assessment for nuclear power plants in Switzerland. *Proceedings of the Twelfth European Conference on Earthquake Engineering*, London, paper no. 633.

Ahorner, L. (1983) Historical seismicity and present-day microearthquake activity of the rhenisch massif, central Europe, in: Plateau Uplift – The Rhenish Massif, A case history, Fuchs, K., K. von Gehlen, H. Maelzer, H. Murawski and A. Semmel eds., 198-221.

Archuleta, R. J., E. Cranswick, C. Mueller, and P. Spudich (1982). Source parameters of the 1980 Mammoth Lakes, California, earthquake sequence, *J. Geophys. Res.* **87**, 4595-4607.

Atkinson, G. M., and D. M. Boore (2006). Earthquake ground-motion prediction equations for eastern North America, *Bull. Seismol. Soc. Am.* **96**, 2181-2205.

Bakun, W. H., and A. G. Lindh (1977). Local magnitudes, seismic moments, and coda durations for earthquakes near Oroville, California, *Bull. Seismol. Soc. Am.* **67**, 615-629.

Bakun, W. H. and W. B. Joyner (1984). The $M_L$ scale in central California, *Bull. Seismol. Soc. Am.* **74**, 1827-1843.

Bindi, D., D. Spallarossa, C. Eva, and M. Cattaneo (2005). Local and duration magnitudes in northwestern Italy, and seismic moment versus magnitude relationships, *Bull. Seismol. Soc. Am.* **95**, 592-604.

Boatwright, J. (1978). Detailed spectral analysis of two small New York State earthquakes, *Bull. Seismol. Soc. Am.* **68**, 1117-1131.

Bolt, B. A., and M. Herraiz (1983). Simplified estimation of seismic moment from seismograms, *Bull. Seismol. Soc. Am.* **73**, 735-748.

Bommer, J.J., K.J. Coppersmith, R.T. Coppersmith, K.L. Hanson, A. Mangongolo, J. Neveling, E.M. Rathje, A. Rodriguez-Marek, F. Scherbaum, R. Shelembe, P.J. Stafford & F.O. Strasser (2015). A SSHAC Level 3 probabilistic seismic hazard analysis for a new-build nuclear site in South Africa. *Earthq. Spectra* **31**(2), 661-698.

Bommer, J.J. & H. Crowley (2017). The purpose and definition of the minimum magnitude limit in PSHA calculations. *Seism. Res. Lett.* **88**(4), 1097-1106.

Bommer, J.J., B. Dost, B. Edwards, P.P. Kruiver, M. Ntinalexis, A. Rodriguez-Marek, P.J. Stafford and J. van Elk (2017a). Developing a model for the prediction of ground motions due to earthquakes in the Groningen gas field. *Netherlands Journal of Geosciences* **96**(S), s203-s213, DOI: 10.1017/njg.2017.28.

Bommer, J. J., P. J. Stafford, B. Edwards, B. Dost, E. van Dedem, A. Rodriguez-Marek, P. Kruiver, J. van Elk, D. Doornhof, and M. Ntinalexis (2017b). Framework for a ground-motion model for induced seismic hazard and risk analysis in the Groningen gas field, the Netherlands, *Earthq. Spectra* **33** (2), 481-498.

Boore, D. M. (1989). The Richter scale: its development and use for determining earthquake source parameters, *Tectonophysics* **166**, 1-14.

Boore, D.M. and J. Boatwright (1984). Average body-wave radiation coefficients, *Bull. Seismol. Soc. Am.* **74**, 1615-1621.

Bourne, S.J., S.J. Oates, J. van Elk and D. Doornhof (2014). A seismological model for earthquakes induced by fluid extraction from a subsurface reservoir. *J. of Geophys. Res.* **119,** 8991-9015, DOI: 10.1002/201JB011663.

Bourne, S.J.., S.J. Oates, J.J. Bommer, B. Dost, J. van Elk, and D. Doornhof (2015). A Monte Carlo method for probabilistic hazard assessment of induced seismicity due to conventional natural gas production, *Bull. Seismol. Soc. Am.* **105**, 1721-1738.

Braunmiller, J., N. Deichmann, D. Giardini, S. Wiemer, and S. M. W. Grp (2005). Homogeneous moment-magnitude calibration in Switzerland, *Bull. Seismol. Soc. Am.* **95**, 58-74.

Brune, J. N. (1970). Tectonic stress and spectra of seismic shear waves from earthquakes, *J. Geophys. Res.* **75**, 4997-5009.

Brune, J. N. (1971). Correction, *J. Geophys. Res.* **76**, 5002.

Butcher, A., R. Luckett, J.P. Verdon, J.-M. Kendall, B. Baptie, and J. Wookey (2017). Local magnitude discrepancies for near-event receivers: Implications for the U.K. traffic-light scheme. *Bull. Seismol. Soc. Am*. **107** 532-541.

de Lorenzo, S., A. Zollo, and G. Zito (2010). Source, attenuation, and site parameters of the 1997 Umbria-Marche seismic sequence from the inversion of P wave spectra: A comparison between constant Q(P) and frequency-dependent Q(P) models, *J. Geophys. Res.* **115**, DOI: 10.1029/2009jb007004.

Deichmann, N. (2006). Local magnitude, a moment revisited, *Bull. Seismol. Soc. Am.* **96**, 1267-1277.

Deichmann, N. (2017). Theoretical basis for the observed break in ML/MW scaling between small and large earthquakes, *Bull. Seismol. Soc. Am.* **107**, 505-520.

Dost, B. and H. Haak (2002). A comprehensive description of the KNMI seismological instrumentation, KNMI technical report, TR-245, 60pp.

Dost, B., T. Van Eck and H. Haak (2004). Scaling of peak ground acceleration and peak ground velocity recorded in the Netherlands, *Bolletino di Geofisica Teorica ed Applicata* **45**, 153-168.

Dost, B., and H. Haak (2007). Natural and induced seismicity, in Th. E. Wong, D.A.J. Batjes, and J. de Jager, eds., Geology of the Netherlands, Royal Netherlands Academy of Arts and Sciences, 223-239.

Dost, B., E. Ruigrok and J. Spetzler (2017). Development of Seismicity and Probabilistic Seismic Hazard Assessment for the Groningen Gas Field, *Netherlands Journal of Geosciences* **96**(S), s235-s245, DOI: 10.1017/njg.2017.20.

Drouet, S., A. Souriau and F. Cotton (2005). Attenuation, seismic moments, and site effects for weak-motion events: Application to the Pyrenees, *Bull. Seismol. Soc. Am*. **95**, 1731-1785, DOI: 10.1785/0120040105.

Drouet, S., S. Chevrot, F. Cotton, and A. Souriau (2008). Simultaneous inversion of source spectra, attenuation parameters, and site responses: Application to the data of the French accelerometric network, *Bull. Seismol. Soc. Am.* **98**, 198-219.

Drouet, S., F. Cotton, and P. Gueguen (2010). $V_{(S30)}$, kappa, regional attenuation and M-w from accelerograms: application to magnitude 3-5 French earthquakes, *Geophys. J. Int*. **182**, 880-898.

Edwards, B., and J. Douglas (2014). Magnitude scaling of induced earthquakes. *Geothermics* **52**, 132-139.

Edwards, B., B. Allmann, D. Fäh, and J. Clinton (2010). Automatic computation of moment magnitudes for small earthquakes and the scaling of local to moment magnitude, *Geophys. J. Int.* **183**, 407-420.

Edwards, B., and D. Fäh (2013). A stochastic ground-motion model for Switzerland, *Bull. Seismol. Soc. Am.* **103**, 78-98.

Edwards, B., C. Michel, V. Poggi, and D. Fäh (2013). Determination of site amplification from regional seismicity: application to the Swiss national seismic networks, *Seismol. Res. Lett.* **84**, 611-621.

Edwards, B., T. Kraft, C. Cauzzi, P. Kästli, and S. Wiemer (2015). Seismic monitoring and analysis of deep geothermal projects in St Gallen and Basel, Switzerland, *Geophys. J. Int.* **201**, 1020-1037.

Edwards, B., A. Rietbrock, J. J. Bommer, and B. Baptie (2008). The acquisition of source, path, and site effects from microearthquake recordings using Q tomography: Application to the United Kingdom, *Bull. Seismol. Soc. Am.* **98**, 1915-1935.

Fäh, D., Giardini, D., Bay, F., Bernardi, F., Braunmiller, J., Deichmann, N. et al. (2003). Earthquake Catalogue Of Switzerland (ECOS) and the related macroseismic database. Eclogae Geologicae Heltveticae. *Swiss Journal of Geosciences* **96**, 219-236, DOI:10.1007/s00015-003-1087-0.

Fäh, D., D. Giardini, P. Kästli, N. Deichmann, M. Gisler, G. Schwarz-Zanetti, S. Alvarez-Rubio, S. Sellami, B. Edwards, and B. Allmann (2011). ECOS-09 Earthquake Catalogue of Switzerland Release 2011 Report and Database. Public catalogue, 17. 4. 2011. Swiss Seismological Service ETH Zurich, 42.

Fletcher, J., J. Boatwright, L. Haar, T. Hanks, and A. Mcgarr (1984). Source parameters for aftershocks of the Oroville, California, earthquake, *Bull. Seismol. Soc. Am.* **74**, 1101-1123.

Goertz-Allmann, B. P., B. Edwards, F. Bethmann, N. Deichmann, J. Clinton, D. Fäh, and D. Giardini (2011). A new empirical magnitude scaling relation for Switzerland, *Bull. Seismol. Soc. Am*. **101**, 3088-3095.

Grünthal, G., and R. Wahlstrom (2012). The European-Mediterranean earthquake catalogue (EMEC) for the last millennium, *J. Seismol.* **16**, 535-570.

Grünthal, G., R. Wahlstrom, and D. Stromeyer (2009). The unified catalogue of earthquakes in central, northern, and northwestern Europe (CENEC)-updated and expanded to the last millennium, *J. Seismol.* **13**, 517-541.

Grünthal, G., R. Wahlstrom, and D. Stromeyer (2013). The SHARE European Earthquake Catalogue (SHEEC) for the time period 1900-2006 and its comparison to the European-Mediterranean Earthquake Catalogue (EMEC), *J. Seismol.* **17**, 1339-1344.

Hanks, T. C., and D. M. Boore (1984). Moment-magnitude relations in theory and practice, *J. Geophys. Res.* **89**, 6229-6235.

Hanks, T. C., and H. Kanamori (1979). Moment magnitude scale, *J. Geophys. Res.* **84**, 2348-2350.

Johnson, L. R., and T. V. Mcevilly (1974). Near-field observations and source parameters of Central California earthquakes, *Bull. Seismol. Soc. Am.* **64**, 1855-1886.

Kanamori, H. (1977). Energy-release in Great Earthquakes, *J. Geophys. Res.* **82**, 2981-2987.

Kanamori, H., J. Mori, E. Hauksson, T.H. Heaton, L.K. Hutton and L.M. Jones (1993). Determination of earthquake energy release and $M_L$ using terrascope, *Bull. Seismol. Soc. Am.* **83**, 330-346.

Kraaijpoel, D. and B. Dost (2013). Implications of salt-related propagation and mode conversion effects on the analysis of induced seismicity, *J. Seismol*. **17**, 95-107.

Kruiver, P. P., E. van Dedem, E. Romijn, G. de Lange, M. Korff, J. Stafleu, J.L. Gunnink., A. Rodriguez-Marek, J.J. Bommer, JJ. van Elk & D. Doornhof (2017). An integrated shear-wave velocity model for the Groningen gas field, The Netherlands. *Bull. Earthq. Eng.* ***15***, 3555-3580, DOI: 10.1007/s10518-017-0105-y.

Margaris, B. N., and C. B. Papazachos (1999). Moment-magnitude relations based on strong-motion records in Greece, *Bull. Seismol. Soc. Am.* **89** 442-455.

Munafò, I., L. Malagnini, and L. Chiaraluce (2016). On the relationship between $M_w$ and $M_L$ for small earthquakes, *Bull. Seismol. Soc. Am.* **106**, 2402-2408.

NAM, (2016). Technical addendum to Winningsplan, online at: http://www.nam.nl/algemeen/mediatheek-en-downloads/winningsplan-2016.html, last accessed: 27/7/17.

Renault, P., Heuberger, S. & Abrahamson, N.A. (2010). PEGASOS Refinement Project: An improved PSHA for Swiss nuclear power plants. *Proceedings of the 14th European Conference of Earthquake Engineering*, Ohrid, Republic of Macedonia, Paper ID 991.

Richter, C. F. (1935). An instrumental earthquake magnitude scale, *Bull. Seismol. Soc. Am.* **25**, 1-32.

Rietbrock, A., F. Strasser, and B. Edwards (2013). A stochastic earthquake ground-motion prediction model for the United Kingdom, *Bull. Seismol. Soc. Am.* **103**, 57-77.

Rodriguez-Marek, A., P.P. Kruiver, P. Meijers, J.J. Bommer, B. Dost, J. van Elk & D. Doornhof (2017). A regional site-response model for the Groningen gas field. *Bull. Seismol. Soc.Am.*, **107**(5), 2067-2077, DOI: 10.1785/0120160123.

Roumelioti, Z., C. Benetatos, and A. Kiratzi (2009). The 14 February 2008 earthquake (M6.7) sequence offshore south Peloponnese (Greece): Source models of the three strongest events, *Tectonophysics* **471**, 272-284.

Sargeant, S., and L. Ottemoller (2009). Lg wave attenuation in Britain, *Geophys. J. Int.* **179**, 1593-1606.

Savage, M. K. and J. G. Anderson (1995). A local-magnitude scale for the Western Great Basin-Eastern Sierra Nevada from synthetic Wood-Anderson seismograms, *Bull. Seismol. Soc. Am.* **85**, 1236-1243.

Spetzler, J. and B. Dost (2017a). Hypocenter estimation of induced earthquakes in Groningen, *Geophys. J. Intl*. **209**, 453-465, DOI: 10.1093/gji/ggx020.

Spetzler, J. and B. Dost (2017b) Probabilistic Seismic Hazard Analysis for Induced Earthquakes in Groningen; Update June 2017. *KNMI report*.

Thatcher, W., and T. C. Hanks (1973). Source parameters of Southern-California earthquakes, *J. Geophys. Res.* **78**, 8547-8576.

USNRC (2012). Central and Eastern United States Seismic Source Characterization for Nuclear Facilities, NUREG-2115, US Nuclear Regulatory Commission, Washington D.C.

Woessner, J., D. Laurentiu, D. Giardini, H. Crowley, F. Cotton, G. Grünthal, G. Valensise, R. Arvidsson, R. Basili, and M. B. Demircioglu (2015). The 2013 European seismic hazard model: key components and results, *Bulletin of Earthquake Engineering* **13,** 3553-3596.

Zollo, A., A. Orefice, and V. Convertito (2014). Source parameter scaling and radiation efficiency of microearthquakes along the Irpinia fault zone in southern Apennines, Italy, *J. Geophys. Res.* **119**, 3256-3275.

## Author Mail Addresses

Dost: Royal Netherlands Meteorological Institute, Utrechtseweg 297, NL-3731 GA De Bilt, Netherlands

Edwards: Department of Earth, Ocean and Ecological Sciences, 4 Brownlow Street, University of Liverpool, Liverpool L69 3GP, U.K.

Bommer: Department of Civil & Environmental Engineering, Imperial College London, London SW7 2AZ, U.K.

## Figure Captions

Figure 1. Networks in Groningen. In red (inverted triangles) Assen network (1988-1994), in red (triangles) borehole network (1995-present), orange: additions in 2010, blue: additions since 2015, green: accelerometers, grey areas: gas fields, blue lines: coast lines and lake contours. The region of interest is marked in red on the map of Europe in the inset.

Figure 2. Difference between calculated station magnitude and average magnitude (dM) for events recorded in the period 2010-2015 as a function of hypocentral distance. Mean values are indicated in blue.

Figure 3: Example of data processing and inversion. Top: acceleration data (east-west and north-south); Middle: Fourier spectrum (blue), model fit (red) and noise (green), logarithmic frequency axis. Bottom: as middle, now showing a linear frequency-axis.

Figure 4. Distance dependence of the normalized low-frequency spectral level for Groningen events listed in Table S1, available in the electronic supplement to this article. The solid and dashed lines show the best fitting decay rate and 95 % confidence interval, respectively.

Figure 5. PGV as a function of distance for the Groningen area near Zeerijp (Ewoud van Dedem, personal comm.). Binned data is shown in blue, average values in green. Fits to particular distance ranges are shown along with the 1/R line for reference.

Figure 6. Comparison of **M** determined using the approach detailed here, and those calculated following the approach detailed in Edwards et al. (2010).

Figure 7. Moment magnitude **M** as a function of local magnitude $M_L$. In green the proposed quadratic relation is shown [Equation (14)]. In red-dashed the Grünthal et al. (2009) relation and in blue the Munafò et al., (2016) relation. Error bars indicate the standard deviation of the magnitudes.

Figure 8. Difference between station moment magnitude and average moment magnitude for four stations. All stations show an average (mu) around zero, only BHKS and BAPP show a positive bias. *N* indicates the number of events, *std* the standard deviation.

Figure 9. Amplification at four sites as shown in Figure 9. Amplification is estimated using 1D-SH transfer functions (red, Rodriguez-Marek et al., 2017) and the empirical spectral model (median: blue; standard deviation: light-blue; Edwards et al., 2013; Bommer et al., 2017b). The square-root impedance amplification level (200 m/s site and 2000 m/s source, as per typical conditions) is indicated by the green line.

Figure 10. Comparison of several regional studies between ML and M (Archuleta *et al.,* 1982; Bakun and Lindh, 1977; Bindi *et al.,* 2005; Bolt and Herraiz, 1983; Drouet *et al.,* 2008; Edwards *et al.,* 2008; Fletcher *et al.,* 1984; Johnson and McEvilly, 1974; Margaris and Papazachos, 1999; Roumelioti *et al.,* 2009; Sargeant and Ottemoller, 2009; Thatcher and Hanks, 1973; Zollo *et al.,* 2014). Grünthal et al. (2009) and Edwards et al. (2015) span the complete magnitude range – based on either data or theoretical considerations.

Figure 11. $M_L$ calculated for events of magnitude **M** simulated with the Groningen GMM (Bommer et al., 2017b) at the reference rock horizon. Grey: 7MPa, blue 14 MPa. Red line: M:$M_L$ equation.

## Figures

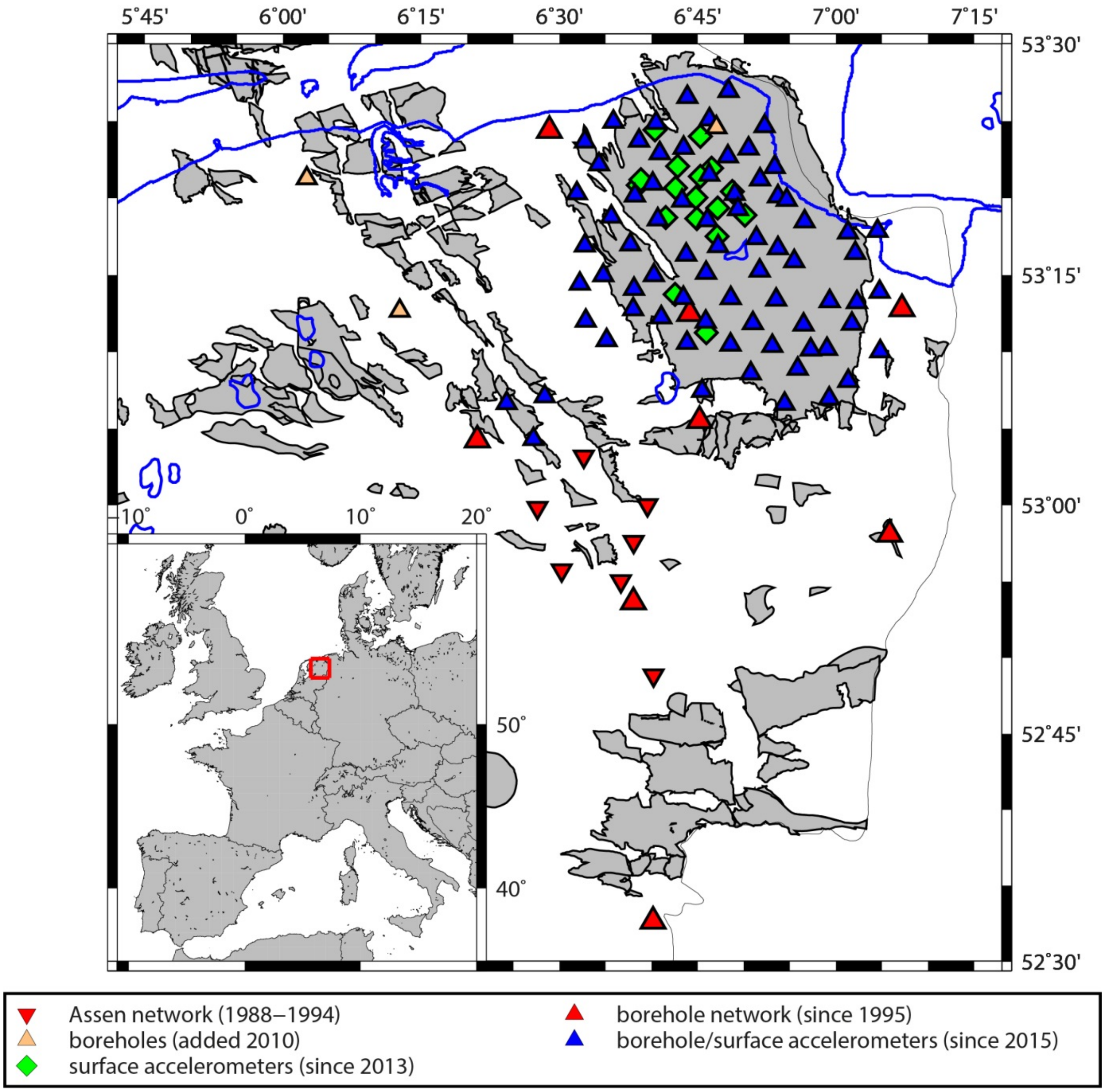


Figure 1. Networks in Groningen. In red (inverted triangles) Assen network (1988-1994), in red (triangles) borehole network (1995-present), orange: additions in 2010, blue: additions since 2015, green: accelerometers, grey areas: gas fields, blue lines: coast lines and lake contours. The region of interest is marked in red on the map of Europe in the inset.

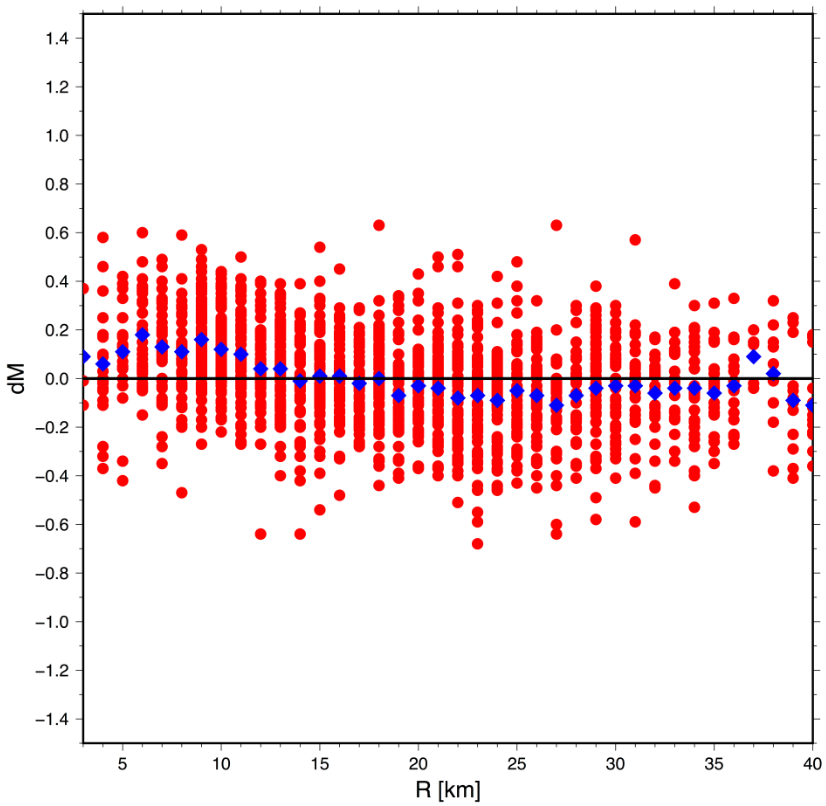


Figure 2. Difference between calculated station magnitude and average magnitude (dM) for events recorded in the period 2010-2015 as a function of hypocentral distance. Mean values are indicated in blue.

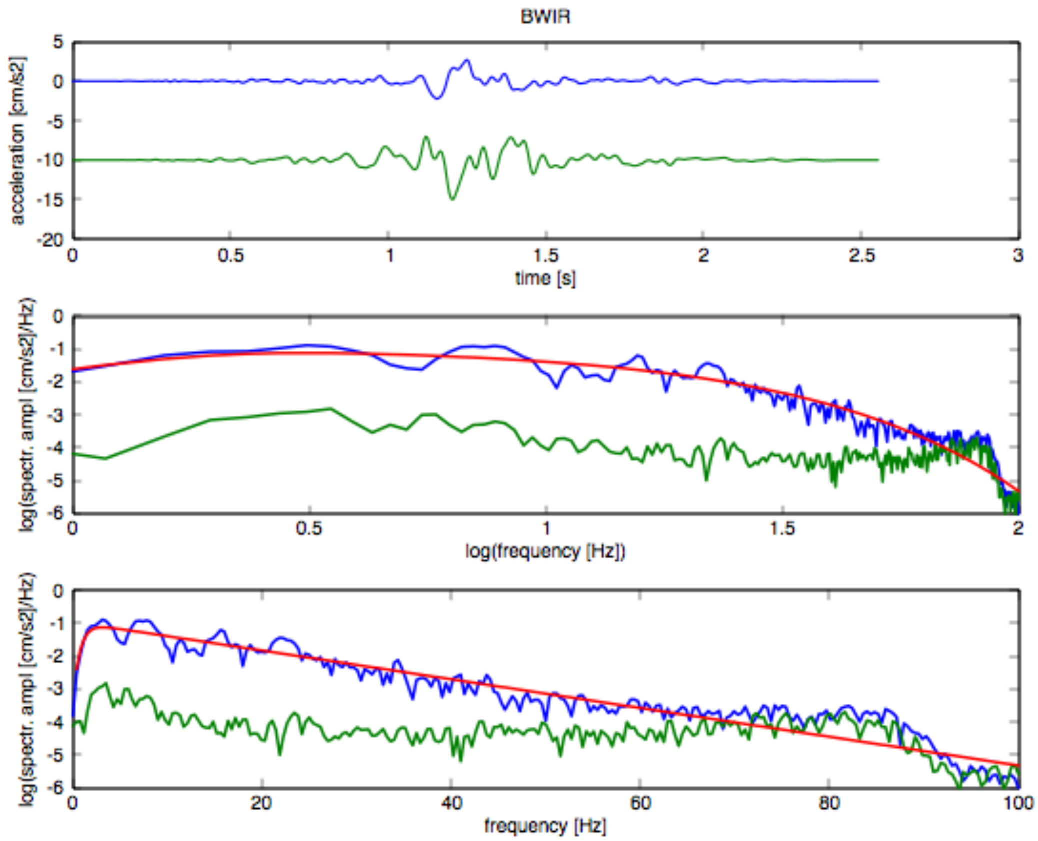


Figure 3: Example of data processing and inversion. Top: acceleration data (east-west and north-south); Middle: Fourier spectrum (blue), model fit (red) and noise (green), logarithmic frequency axis. Bottom: as middle, now showing a linear frequency-axis.

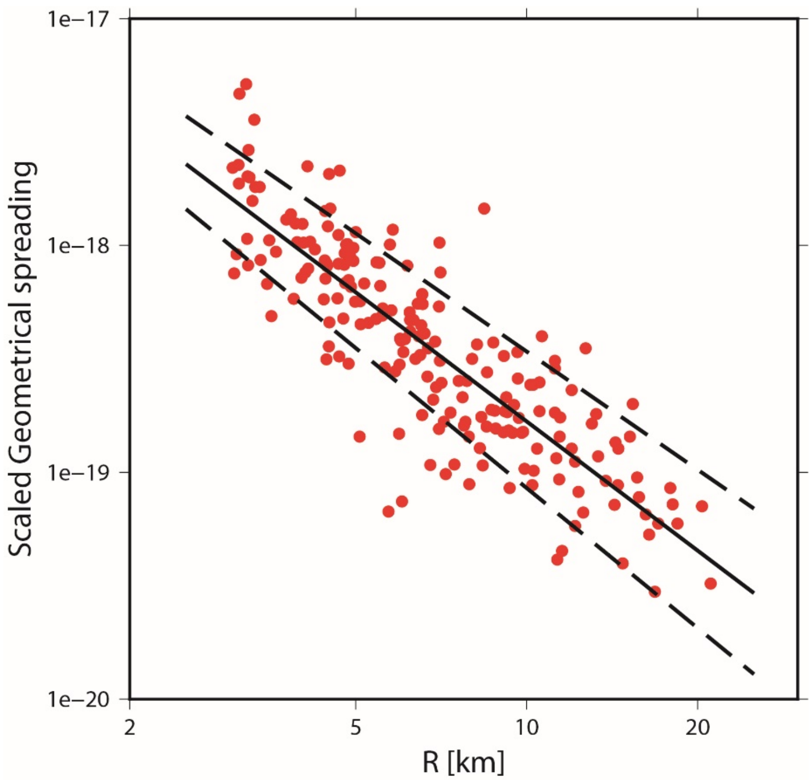


Figure 4. Distance dependence of the normalized low-frequency spectral level for Groningen events listed in Table S1, available in the electronic supplement to this article. The solid and dashed lines show the best fitting decay rate and 95 % confidence interval, respectively.

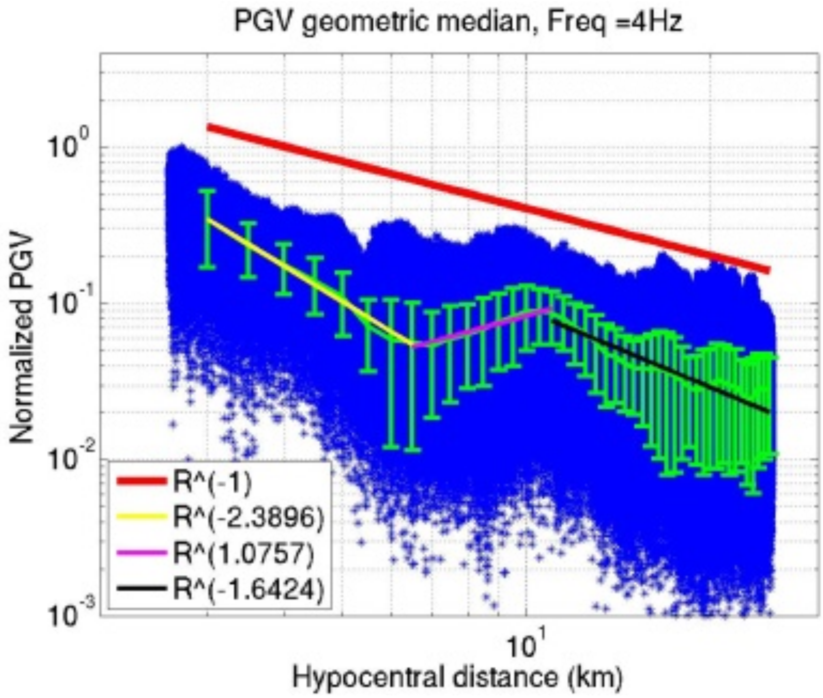


Figure 5. PGV as a function of distance for the Groningen area near Zeerijp (Ewoud van Dedem, personal comm.). Binned data is shown in blue, average values in green. Fits to particular distance ranges are shown along with the 1/R line for reference.

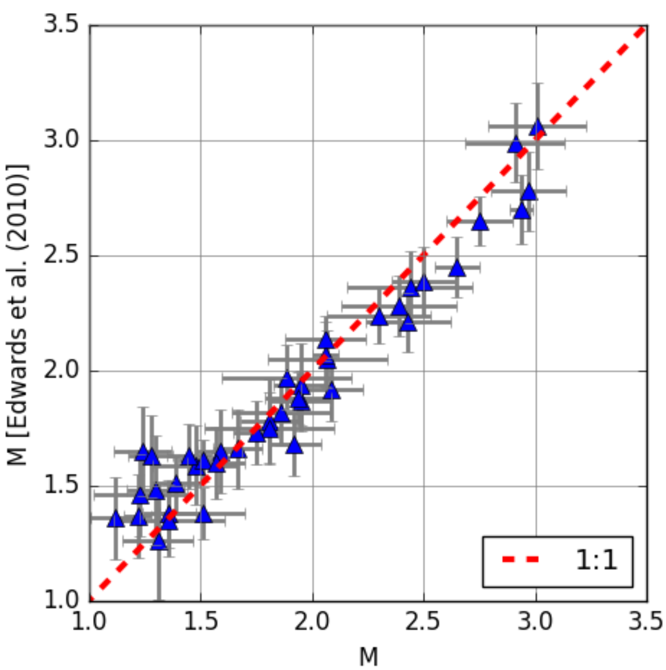

Figure 6. Comparison of **M** determined using the approach detailed here, and those calculated following the approach detailed in Edwards et al. (2010).

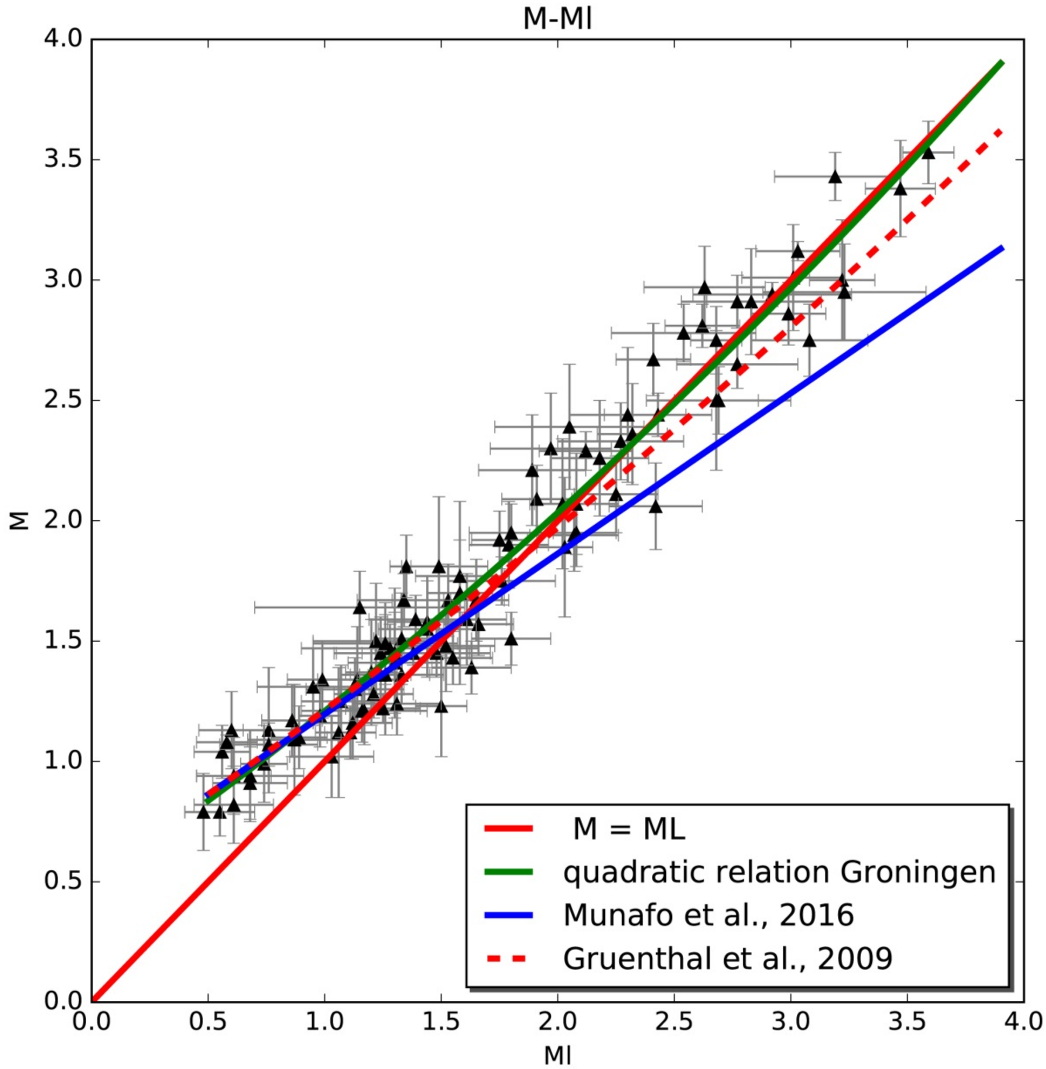


Figure 7. Moment magnitude **M** as a function of local magnitude $M_L$. In green the proposed quadratic relation is shown [Equation (14)]. In red-dashed the Grünthal et al. (2009) relation and in blue the Munafò et al., (2016) relation. Error bars indicate the standard deviation of the magnitudes.

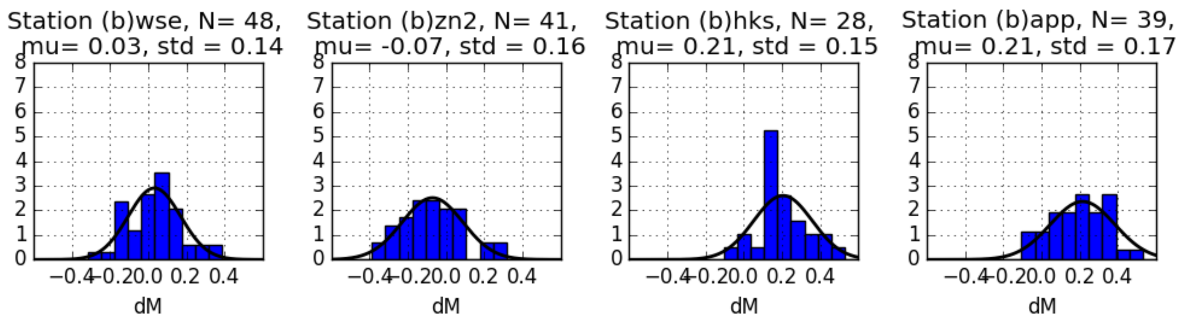


Figure 8. Difference between station moment magnitude and average moment magnitude for four stations. All stations show an average (mu) around zero, only BHKS and BAPP show a positive bias. *N* indicates the number of events, *std* the standard deviation.

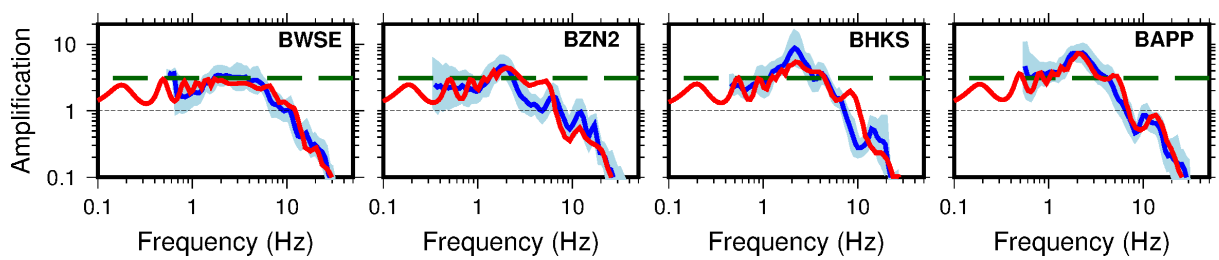


Figure 9. Amplification at four sites as shown in Figure 9. Amplification is estimated using 1D-SH transfer functions (red, Rodriguez-Marek et al., 2017) and the empirical spectral model (median: blue; standard deviation: light-blue; Edwards et al., 2013; Bommer et al., 2017b). The square-root impedance amplification level (200 m/s site and 2000 m/s source, as per typical conditions) is indicated by the green line.

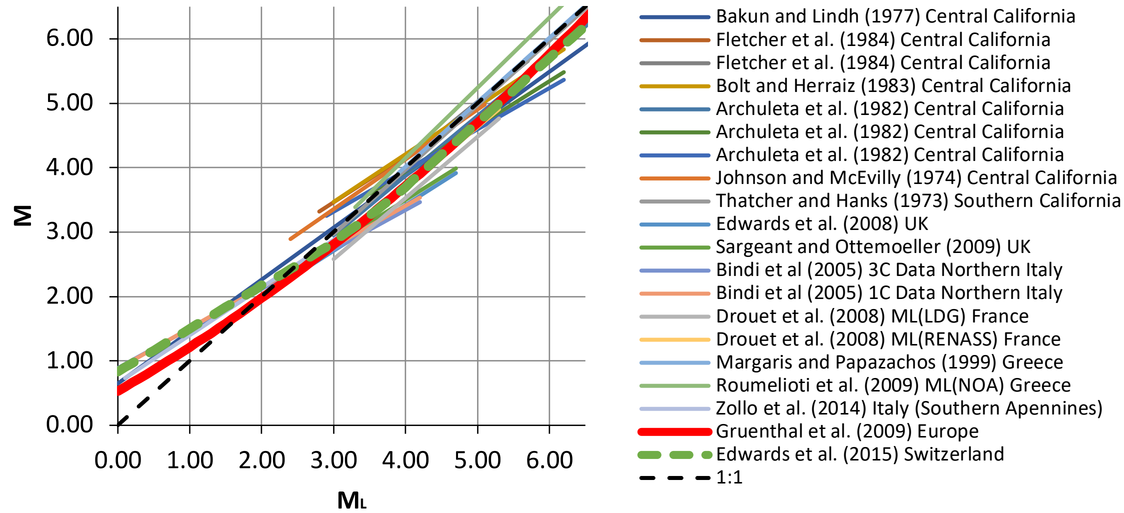


Figure 10. Comparison of several regional studies between $M_L$ and **M** (Archuleta *et al.,* 1982; Bakun and Lindh, 1977; Bindi *et al.,* 2005; Bolt and Herraiz, 1983; Drouet *et al.,* 2008; Edwards *et al.,* 2008; Fletcher *et al.,* 1984; Johnson and McEvilly, 1974; Margaris and Papazachos, 1999; Roumelioti *et al.,* 2009; Sargeant and Ottemoller, 2009; Thatcher and Hanks, 1973; Zollo *et al.,* 2014). Grünthal et al. (2009) and Edwards et al. (2015) span the complete magnitude range – based on either data or theoretical considerations.

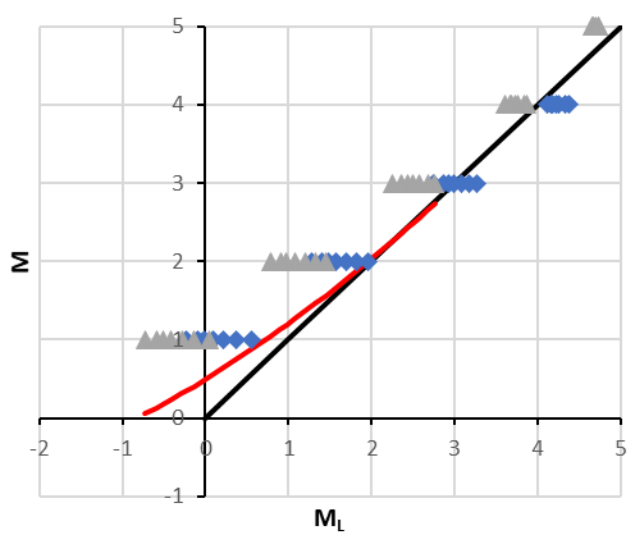

Figure 11. $M_L$ calculated for events of magnitude **M** simulated with the Groningen GMM (Bommer et al., 2017b) at the reference rock horizon. Grey: 7MPa, blue 14 MPa. Red line: $M$:$M_L$ equation.